

Numerical study of subcritical Rayleigh-Bénard convection rolls in strongly shear-thinning Carreau fluids[☆]

Mathieu Jenny^{a,*}, Emmanuel Plaut^a, Antoine Briard^{a,b}

^a*Université de Lorraine, Laboratoire d’Énergétique et de Mécanique Théorique et Appliquée, UMR CNRS 7563, Vandoeuvre-lès-Nancy, F-54500, France*

^b*Université Pierre et Marie Curie, Institut Jean le Rond d’Alembert, UMR CNRS 7190, 4 place Jussieu 75252 Paris Cedex 05, France*

Abstract

The Rayleigh-Bénard thermoconvection of Newtonian fluids has been extensively studied. The transition from the conductive, static state to thermoconvection flows corresponds in this case to a supercritical bifurcation. In shear-thinning fluids, on the contrary, recent weakly nonlinear studies have shown that the transition may become subcritical. Using a custom numerical code developed with Freefem++ to compute bidimensional, fully nonlinear roll solutions in Carreau fluids, for a large range of rheological parameters, and more particularly for strongly shear-thinning fluids, approaching power-law fluids, we confirm this result. A simple expression of the value of the Rayleigh number at which subcritical convection rolls appear is proposed. This law suggests to reconsider the choice of the reference viscosity for shear-thinning fluids. Indeed, when the shear-thinning effects increase, the critical Rayleigh number increases or decreases depending on the choice of the reference viscosity. The ‘neutral’ or ‘effective’ viscosity, which gives a constant value of the Rayleigh number at the onset of subcritical convection rolls, is close to the bulk average viscosity. In addition, a correlation is proposed to estimate the Nusselt number of subcritical

[☆]Emmanuel Plaut’s home page.

*Corresponding author

Email addresses: mathieu.jenny@univ-lorraine.fr (Mathieu Jenny),
emmanuel.plaut@univ-lorraine.fr (Emmanuel Plaut)

rolls.

Keywords: Rayleigh-Bénard convection, Non-Newtonian fluids, Subcritical instability

2010 MSC: 76A05, 76D99, 76E06, 76E30

1. Introduction

Rayleigh-Bénard thermoconvection constitutes a paradigmatic system that is extensively studied because of its academical and practical interest. For recent reviews, see [1, 2]. A temperature gradient in a viscous fluid produces differences of density, and a buoyancy-driven instability may set in, that leads to thermoconvection flows. The transition from the conductive, static state to thermoconvection flows occurs when the buoyancy becomes strong enough to overcome the stabilizing effects of viscous and thermal diffusions, *i.e.*, when the Rayleigh number

$$R = \rho_0 g \beta \delta T d^3 / (\eta_0 \kappa) \quad (1)$$

is large enough. Here, ρ_0 is the reference value of the density, g the acceleration due to gravity, β the thermal expansion coefficient, δT the temperature difference between the bottom and top walls separated by a distance d (Fig. 1), η_0 the reference value of the dynamic viscosity, κ the thermal diffusivity. In systems extended in the horizontal directions, and with realistic no-slip boundary conditions at the horizontal walls, which are the ones on which we focus, for a Newtonian fluid, the static state becomes linearly unstable above the critical Rayleigh number $R_c = R_c^{\text{Newt}} = 1707.8$ (see e.g. [3]). The bifurcation is supercritical: if $R < R_c$, an initial flow will decay, if $R > R_c$, thermoconvection flows develop smoothly. This bifurcation is also pattern-forming: in the absence of sidewall forcing, for R slightly larger than R_c , the thermoconvection flows are generally straight rolls, of horizontal wavenumber k close to the critical value $k_c = 3.116/d$ [1, 3]. Such two-dimensional rolls are interesting because they constitute the simplest thermoconvection flows that can exist in this setup, but present some qualitative or semi-quantitative features that persist at higher

Rayleigh numbers and in more complex flows. For instance, two-dimensional rolls increase heat transfer, as measured by the Nusselt number Nu which is the ratio of the heat flux transferred by conduction and convection to the heat flux that would be transferred by conduction only, at the same value of δT . The Nusselt number is larger at large Prandtl number

$$P = \eta_0 / (\rho_0 \kappa) , \quad (2)$$

as it can be seen for straight rolls near onset, of wavenumber $k = k_c$, by studying the weakly nonlinear formula

$$Nu - 1 = \frac{1}{0.69942 - 0.00472P^{-1} + 0.00832P^{-2}} \frac{R - R_c}{R} \quad (3)$$

derived by [3]. The same tendency exists in turbulent convection, observe the Fig. 5a of [2]. From the formula (3) and this figure, one can define ‘large P ’ by $P \gtrsim 1$, which is the case that corresponds to most liquids for standard conditions, and that will be considered here.

Whereas thermoconvection rolls and their onset in Newtonian fluids have been precisely characterized and are well known [1, 3, 4], in non-Newtonian fluids the situation is more complex. Firstly, there can exist elastic effects, as described for instance by [5], or compositional effects, as advocated by [6]. Hereafter, we will focus instead on shear-thinning effects, which are quite common in non-Newtonian fluids. We will neglect the elastic response of the fluid, as well as compositional effects.

Even in this framework, the problem of the onset of convection can be puzzling. For quite strongly shear-thinning fluids like yield-stress fluids, there is still a debate on this subject, as exemplified by the different experimental results obtained recently by [7, 8]. Hereafter, we choose to study shear-thinning fluids without yield-stress. An interesting example of such fluids is given by the power-law fluids. Their rheology is characterized by two parameters only, the consistency M and the shear-thinning index n_i , $n_i \in [0, 1[$, such that the dynamic viscosity

$$\eta = M (\dot{\gamma})^{n_i-1} \quad (4)$$

with $\dot{\gamma}$ the rate of strain. Because of their simplicity, these models are often used in the Engineering community and also by some Researchers. However, the theoretical literature concerning Rayleigh-Bénard convection of power-law fluids in extended geometry is sparse. In fact, to our knowledge, as far as convection rolls in extended geometry are concerned, the relevant articles are [9, 10, 11, 12]. Eq. (4) shows that, at rest, $\dot{\gamma} = 0$, the viscosity diverges: it is therefore clear that the conduction state is linearly stable, i.e., that the onset of convection flows occurs through a nonlinear instability. Following [9], it is natural to define a Rayleigh number by estimating the viscosity at a rate of strain which is the inverse of the thermal diffusion time

$$\tau_{\text{th}} = d^2/\kappa, \quad (5)$$

i.e.

$$Ra = \rho_0 g \beta \delta T d^3 / [M(\tau_{\text{th}})^{1-n_i} \kappa] = \rho_0 g \beta \delta T d^{2n_i+1} / (M \kappa^{n_i}). \quad (6)$$

Ozoe & Churchill [9] solved with a finite-difference method the system of equations of Boussinesq convection in a power-law fluid, in a two-dimensional xy square cell with ‘dragless vertical boundaries’. The boundary conditions at $x = 0$ and d were that the heat flux and the viscous stress vanish. These conditions corresponds to the ones insured by the symmetries of thermoconvection rolls, of wavelength $2d$ i.e. wavenumber $k = \pi/d$, with separatrices at $x = 0$ and d : this cell corresponds to one roll of a regular pattern. Hence, with this method, an ‘extended geometry’ can be studied without Fourier expansion, and with computations in a small domain. Hereafter, we adopt the same strategy, except that we choose a rectangular cell corresponding to the critical wavenumber, i.e., the length of the cell in the horizontal x direction is $L_x = \pi/k_c = 1.008d$. Starting with Newtonian solutions ($n_i = 1$) at large Rayleigh number, and decreasing n_i and Ra by steps, [9] determined a (sub)critical value of Ra below which the flow vanished. We denote this Ra_{sc} (not Ra_c) since it corresponds (roughly, i.e., within the size of the last step in Ra) to the smallest subcritical value of Ra at which convection rolls can be sustained, i.e. to the position of the turning point - saddle-node bifurcation at which the roll branch solution

disappears. This subcritical value Ra_{sc} was found to decrease from R_c^{Newt} to 250, as the shear-thinning index n_i decreased from 1 to 0.5, see their Fig. 20. In [10], a correlation was also developed to estimate the maximum rate of strain and the Nusselt number in convection rolls in power-law fluids. This correlation is rather complex and cannot be casted in a single formula, see the Page 131 of [10]. Another interesting correlation has been proposed by Parmentier [11], who studied in some details nonlinear convection rolls above onset in power-law fluids, with a geometry and numerical method similar to the ones used by [9, 10]. Parmentier [11] introduced an average viscosity, that we will denote η_P , which is a volume average of the viscosity η weighted by the square of the rate of strain $(\dot{\gamma})^2$. He showed, on the basis of a few computations, that, if one uses a ‘Parmentier-Rayleigh number’

$$Ra_P = \rho_0 g \beta \delta T d^3 / (\eta_P \kappa), \quad (7)$$

then the Nusselt number Nu vs Ra_P data points fall on a universal curve, which is the curve $Nu(Ra)$ of the convection rolls in a Newtonian fluid. Thus, the ‘Parmentier viscosity’ η_P is the relevant viscosity to characterize the heat transfers. An unphysical feature of the power-law model is the infinite value of the viscosity at zero rate of strain. Therefore, in the numerical models of [9, 10, 11], various regularizations were used. Because of this, the behaviour of their solutions in the vicinity of the space points where $\dot{\gamma} = 0$ (at the corners of the rolls, or at some particular points on the separatrices between rolls) is questionable. A quite physical regularization of the power-law model is offered by the Carreau model

$$\eta = \eta_0 (1 + \lambda^2 \dot{\gamma}^2)^{(n_i - 1)/2} \quad (8)$$

which is considered here with a vanishing viscosity at infinite rate of strain. This rheological model has a theoretical basis [13] and describes the viscosity of several real fluids, like polymer solutions, over a quite large range of values of $\dot{\gamma}$, as shown for instance in [14]. As compared with the power-law model, a new parameter comes in: the characteristic time of the fluid λ . Its inverse $1/\lambda$ gives the characteristic rate of strain above which the viscosity (8) starts

to decrease below the Newtonian plateau $\eta = \eta_0$. A dimensionless measure of the characteristic time is, naturally,

$$\lambda_a = \lambda/\tau_{\text{th}} = \lambda\kappa/d^2 . \quad (9)$$

Clearly, when $\lambda \rightarrow +\infty$, the Carreau model (8) approaches the power-law model (4) with

$$M = M_C = \eta_0 \lambda^{n_i-1} . \quad (10)$$

To our knowledge, Rayleigh-Bénard convection in Carreau fluids has only been studied on the basis of linear and weakly nonlinear methods, i.e., near onset. Since, in the vicinity of the conduction static state, Eq. (8) gives $\eta = \eta_0 + O(\dot{\gamma}^2)$, the linear problem in a Carreau fluid is analogous to the linear problem in a Newtonian fluid: the linear onset in terms of the Rayleigh number (1) is still at $R_c = R_c^{\text{Newt}}$. Using stress-free boundary conditions at the horizontal walls, [15, 16] showed that the effect of the nonlinearity in Eq. (8) is to change the bifurcation from supercritical to subcritical, if the fluid is sufficiently shear-thinning, as it will be precised in Eq. (27) below. These computations have been also made with no-slip boundary conditions at the horizontal walls by [17]. The same phenomenon occurs, though the critical values of the rheological parameters at which the bifurcation to rolls changes of nature is modified (again, see Eq. 27 below). Moreover, [17] also demonstrated that, in the supercritical regime and near onset, two-dimensionnal rolls are stable vs simple perturbations that could lead to three-dimensional patterns, ‘square’ or ‘hexagons’.

The aim of the present article is to study strongly subcritical Boussinesq convection rolls in Carreau fluids, on the basis of a finite-element code constructed with Freefem++ by Hecht [18]. As already discussed, the strategy adopted by [9] is used, *i.e.*, we compute only one roll in a row of rolls of critical wavenumber. During the course of this work, we become aware of the recent study [12]. In their section V.G, they study a system quite similar to the one addressed here, except for a slightly smaller aspect ratio. Moreover, they use only one value of λ , $\lambda = 0.4$, whereas we will focus on the limit $\lambda \rightarrow +\infty$: therefore, our results are for interest for Carreau fluids but also for power-law fluids. Nevertheless,

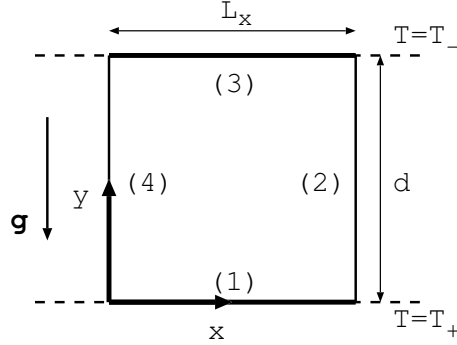


Figure 1: Rayleigh-Bénard geometry: cell of one roll in a row of rolls with wavenumber k . Thus $L_x = \pi/k$.

a comparison with [12] will be shown in section 7. A very good agreement is found. Our computations have been done by using R (1) as the main control parameter. In the limit $\lambda \rightarrow +\infty$, it will be relevant to also use a Rayleigh number constructed with the Eqs. (6) and (10),

$$Ra = \rho_0 g \beta \delta T d^{2n_i+1} / (M_C \kappa^{n_i}) = \rho_0 g \beta \delta T d^{2n_i+1} / (\eta_0 \lambda^{n_i-1} \kappa^{n_i}) = \lambda_a^{1-n_i} R. \quad (11)$$

The plan of this article is as follows. In Section 2, we introduce the equations of the problem. Section 3 summarizes the already known weakly nonlinear results. In Section 4, we describe the numerical methods. The validation of the code is described in Section 5. The results and the effect of a finite viscosity at infinite rate of strain are presented in Sections 6 and 7, which are followed by a concluding discussion.

2. Basic equations in dimensionless units

Consider a shear-thinning fluid in a Rayleigh-Bénard xy geometry (Fig. 1), with the isothermal boundary conditions $T = T_+ = T_0 + (\delta T)/2$ (resp. $T = T_- = T_0 - (\delta T)/2$) at the bottom (resp. top) plate situated at $y = 0$ (resp. d). Denote $T_c = T_+ - (\delta T)(y/d)$ the conductive profile of temperature, at rest. The dimensionless perturbation of temperature is defined by $\theta = (T - T_c)/(\delta T)$.

Using the thermal diffusion time τ_{th} (5) as the time scale, a natural velocity scale is

$$v_{\text{th}} = d/\tau_{\text{th}} = \kappa/d. \quad (12)$$

With the thickness d as the length scale, the dimensionless heat equation reads

$$\frac{\partial \theta}{\partial t} + \mathbf{v} \cdot \nabla \theta = \Delta \theta + \mathbf{v} \cdot \mathbf{e}_y \quad (13)$$

with \mathbf{v} the dimensionless velocity field. Hereafter \mathbf{e}_x and \mathbf{e}_y denote the unit vectors in the directions of the x and y axes (Fig. 1). The dimensionless rate-of-strain tensor is

$$\dot{\bar{\gamma}} = \bar{\nabla} \mathbf{v} + \bar{\nabla} \mathbf{v}^T \quad (14)$$

where \cdot^T denotes the transposition. Its second invariant is the dimensionless rate of strain

$$\dot{\gamma}_a = \left(\frac{1}{2} \dot{\gamma}_{ij} \dot{\gamma}_{ij} \right)^{1/2}. \quad (15)$$

With the viscosity at rest, η_0 , as the scale of viscosity, the dimensionless viscosity of the Carreau model (8) reads

$$\eta_a = \left(1 + \lambda_a^2 \dot{\gamma}_a^2 \right)^{(n_a - 1)/2}. \quad (16)$$

With $\eta_0 \tau_{\text{th}}^{-1} = \eta_0 \kappa / d^2$ as the scale of stress, the dimensionless viscous-stress tensor

$$\bar{\boldsymbol{\tau}} = \eta_a \dot{\bar{\gamma}}. \quad (17)$$

The linear momentum equation, written in dimensionless units and under the Boussinesq approximation, reads

$$P^{-1} \left[\frac{\partial \mathbf{v}}{\partial t} + (\mathbf{v} \cdot \nabla) \mathbf{v} \right] = \mathbf{div}(-\Pi \bar{\mathbf{I}} + \bar{\boldsymbol{\tau}}) + R\theta \mathbf{e}_y \quad (18)$$

with Π the dimensionless perturbation of the pressure, with respect to the static pressure in the conduction state.

At the horizontal boundaries, the sides (1) and (3) of Fig. 1, defined by $x \in [0, L_x]$, $y = 0$ or 1 , with $L_x = 1.008$, we apply isothermal boundary condition on the temperature field, no-slip boundary condition on the velocity field:

$$\theta = 0, \quad (19)$$

$$\mathbf{v} = \mathbf{0}. \quad (20)$$

The vertical sides, (2) and (4) in Fig. 1, defined by $x = 0$ or L_x , $y \in [0, 1]$, are 'virtual' boundaries where the symmetries of the convection rolls impose adiabatic boundary condition on the temperature field, free-slip boundary condition on the velocity field:

$$\nabla\theta \cdot \mathbf{e}_x = 0, \quad (21)$$

$$\mathbf{v} \cdot \mathbf{e}_x = 0, \quad (22)$$

$$\mathbf{e}_y \cdot \bar{\bar{\tau}} \cdot \mathbf{e}_x = 0. \quad (23)$$

Finally, under the Boussinesq approximations, the velocity field also fulfills the 'incompressibility' condition

$$\text{div}(\mathbf{v}) = 0. \quad (24)$$

From now on, we omit the index a in the dimensionless rate of strain, viscosity and characteristic time, which are simply denoted by $\dot{\gamma}$, η and λ .

In the nonlinear computations, the time and velocity scales used internally in the code are different, as it will be discussed in section 4.5.

3. Summary of the known weakly nonlinear results

In [17] it has been shown, with a weakly nonlinear analysis based on a spectral method, that, in this system, the nature of the bifurcation from the conduction state to convection rolls with a critical wavenumber depends on a single rheological coefficient

$$\alpha = \frac{1}{2}(1 - n_i)\lambda^2 \quad (25)$$

which controls the magnitude of the first nonlinear term in the dimensionless viscosity (16),

$$\eta = (1 + \lambda^2 \dot{\gamma}^2)^{(n_i-1)/2} = 1 - \alpha \dot{\gamma}^2 + O(\dot{\gamma}^4). \quad (26)$$

For $P \gtrsim 1$, the bifurcation is

$$\begin{aligned} \text{supercritical if } \alpha < \alpha_c &= 2.15 \cdot 10^{-4}, \\ \text{subcritical if } \alpha > \alpha_c &= 2.15 \cdot 10^{-4}. \end{aligned} \quad (27)$$

In the supercritical regime, the lowest-order version of the formula (3) reads

$$Nu - 1 = \frac{\epsilon}{0.69942 - 0.00472P^{-1} + 0.00832P^{-2}} = \gamma^{\text{Newt}} \epsilon, \quad (28)$$

with ϵ the distance to onset:

$$\epsilon = \frac{R - R_c}{R_c}. \quad (29)$$

The formula (28) has to be corrected as follows for a Carreau fluid:

$$Nu - 1 = \frac{\gamma^{\text{Newt}}}{1 - \alpha/\alpha_c} \epsilon. \quad (30)$$

4. Numerical methods

4.1. Weak formulation

To compute the flow in the cell represented in Fig. 1, FreeFem++ [18] is used. The weak formulation of the equations reads:

$$\begin{aligned} \int_D \left[\frac{\partial \theta}{\partial t} + \mathbf{v} \cdot \nabla \theta \right] \varphi \, d^2x &= \int_D [-\nabla \theta \cdot \nabla \varphi + (\mathbf{v} \cdot \mathbf{e}_y) \varphi] \, d^2x \\ &+ \int_{\partial D} \varphi \nabla \theta \cdot \mathbf{n} \, dl, \end{aligned} \quad (31)$$

$$\begin{aligned} P^{-1} \int_D \left[\frac{\partial \mathbf{v}}{\partial t} + (\mathbf{v} \cdot \nabla) \mathbf{v} \right] \cdot \mathbf{w} \, d^2x &= \int_D \left[\left(\Pi \bar{\mathbf{I}} - \bar{\bar{\tau}} \right) : \bar{\nabla} \mathbf{w} + R \theta \mathbf{e}_y \cdot \mathbf{w} \right] \, d^2x \\ &+ \int_{\partial D} \mathbf{w} \cdot \left(-\Pi \bar{\mathbf{I}} + \bar{\bar{\tau}} \right) \cdot \mathbf{n} \, dl, \end{aligned} \quad (32)$$

$$\int_D q \operatorname{div}(\mathbf{v}) \, d^2x = 0, \quad (33)$$

with $d^2x = dx dy$ the surface element in the cell D , dl the length element along the boundaries ∂D , \mathbf{n} the unit vector normal to the boundaries, pointing outward of the cell. The test functions φ , \mathbf{w} and q are associated to the temperature θ , the velocity vector \mathbf{v} and the pressure Π respectively. One interest of this weak formulation is that, in the energy equation (31), the heat flux through the boundary intervenes, whereas, in the velocity equation (32), the stress at the boundary intervenes. This will facilitate the implementation of the boundary conditions (21) and (23).

4.2. Time discretisation

A semi-implicit time scheme is used. A first order discretisation scheme is sufficient to obtain good results, as it will be shown in the following. Denoting by \mathbf{v}_n and θ_n the velocity and temperature fields at the current time step t_n , we write:

$$\int_D \left[\frac{\theta_{n+1}}{\delta t} \varphi + \nabla \theta_{n+1} \cdot \nabla \varphi \right] d^2x = \int_D \left[\frac{\theta_n}{\delta t} - (\mathbf{v} \cdot \nabla \theta)_n + \mathbf{v}_n \cdot \mathbf{e}_y \right] \varphi d^2x + \int_{\partial D} \varphi \nabla \theta_{n+1} \cdot \mathbf{n} dl, \quad (34)$$

$$\int_D \left[P^{-1} \frac{\mathbf{v}_{n+1}}{\delta t} \cdot \mathbf{w} + \left(-\Pi_{n+1} \bar{\bar{\mathbf{I}}} + \hat{\bar{\bar{\boldsymbol{\tau}}}}_{n+1} \right) : \bar{\bar{\nabla}} \mathbf{w} \right] d^2x = \int_D \left[P^{-1} \left(\frac{\mathbf{v}_n}{\delta t} - ((\mathbf{v} \cdot \nabla) \mathbf{v})_n \right) + R \theta_n \mathbf{e}_y \right] \cdot \mathbf{w} d^2x + \int_{\partial D} \mathbf{w} \cdot \left(-\Pi \bar{\bar{\mathbf{I}}} + \bar{\bar{\boldsymbol{\tau}}} \right)_{n+1} \cdot \mathbf{n} dl, \quad (35)$$

$$\int_D q \operatorname{div}(\mathbf{v}_{n+1}) d^2x = 0. \quad (36)$$

The coupling terms $\mathbf{v}_n \cdot \mathbf{e}_y$ and $R \theta_n \mathbf{e}_y$ are explicit to preserve the symmetry of the linear operator with respect to the couples (θ_{n+1}, φ) and $(\mathbf{v}_{n+1}, \mathbf{w})$. Since the stress tensor $\bar{\bar{\boldsymbol{\tau}}}$ depends nonlinearly of the velocity field, we use the approximation of order one in time $\hat{\bar{\bar{\boldsymbol{\tau}}}}_{n+1} = \eta_n \bar{\bar{\boldsymbol{\gamma}}}_{n+1}$, with η_n the viscosity field at time t_n .

4.3. Space discretisation

A triangular mesh with 40×40 identical rectangles in the cell of Fig. 1, each of them divided into two triangles of equal area, is used in most cases.

A convergence test has also been performed with 60×60 rectangles. Each triangle is defined by the position of its three corner's vertices. Interpolation polynomials are defined in an element such that they are equal to 1 on a specific vertex and zero on the others [18]. The pressure is defined on P1 finite-elements, which means that the interpolation functions are polynomials of degree 1. The temperature and velocity fields are defined on P2 finite-elements, where the interpolation functions are polynomials of degree 2. To define P2 finite-elements, the middle points of each P1 element's edges are added to the corner's vertices, to double the number of 'collocation points' [18].

4.4. Numerical scheme

Considering the N vertices \mathbf{x}_i of the mesh for P1 finite elements and the M vertices \mathbf{x}'_i for P2 finite elements, we define the column vectors

$$Q = [\Pi_{n+1}(\mathbf{x}_1), \dots, \Pi_{n+1}(\mathbf{x}_N)]^T \quad (37)$$

and

$$X = \begin{bmatrix} \theta_{n+1}(\mathbf{x}'_1), \dots, \theta_{n+1}(\mathbf{x}'_M), \\ \mathbf{e}_x \cdot \mathbf{v}_{n+1}(\mathbf{x}'_1), \dots, \mathbf{e}_x \cdot \mathbf{v}_{n+1}(\mathbf{x}'_M), \\ \mathbf{e}_y \cdot \mathbf{v}_{n+1}(\mathbf{x}'_1), \dots, \mathbf{e}_y \cdot \mathbf{v}_{n+1}(\mathbf{x}'_M) \end{bmatrix}^T. \quad (38)$$

By computing Eqs. (34 - 36) for general expressions of Π_{n+1} and $(\theta, \mathbf{v})_{n+1}$, and all possible test functions q and (φ, \mathbf{w}) , among the P1 and P2 functions described before, one can identify matrices A , G and D that represent the left-hand-side linear operator in the equations (34 - 35), the gradient and the divergence, respectively. Thus the matrix form of the problem (34 - 36) reads

$$AX + GQ = B, \quad (39)$$

$$DX = 0. \quad (40)$$

In Eq. (39), B represents all the terms that are known explicitly in the right-hand-side of Eqs. (34-35). The boundary terms are not included, *i.e.*, they are cancelled. Some of them vanish because of the Neumann boundary conditions

(21) and (23), the other ones are taken to be zero because the Dirichlet boundary conditions (19), (20) and (22) are imposed by a penalisation method; some diagonal coefficients of the matrix A are modified accordingly [18]. In the non-Newtonian case, our temporal scheme demands to update A because of the evolution of the viscosity as time goes on. To solve Eqs (39-40), we use the Uzawa algorithm [18]. One computes the velocity and temperature fields given by

$$X = A^{-1}(-GQ + B) \quad (41)$$

using the conjugated gradient algorithm. One then obtains the pressure field by

$$Q = (DA^{-1}G)^{-1}(DA^{-1}B) . \quad (42)$$

The pressure (42) is computed using a customized Cahouet & Chabard preconditioner [19]

$$C^{-1} = \frac{P^{-1}}{\delta t}(DG)^{-1} + \eta_{eq}I \quad (43)$$

where η_{eq} is the constant viscosity of the Newtonian fluid and I the identity $N \times N$ matrix, to insure that

$$C^{-1}(DA^{-1}G) \sim I . \quad (44)$$

In our case, the viscosity of non-Newtonian fluids is not constant and we have to define an average viscosity η_{eq} such as the property (44) is preserved. We find that a good solution is

$$\eta_{eq} = \frac{3\eta_n^{min} + \eta_0}{4}, \quad (45)$$

with $\eta_0 = 1$, η_n^{min} the minimal value of the viscosity over the mesh points at the time step n .

Our time scheme becomes equivalent to a fully implicit time scheme despite the explicit terms when the steady state is reached, as we do not use the

Characteristics-Galerkin method implemented in Freefem++ for the convective terms. Nevertheless, during the transient stages, the time step must verify the CFL condition to insure the accuracy and the numerical stability, because of the explicit inertial terms. Thus, in the following, the time step δt always verifies

$$\delta t \leq \frac{\delta x_{min}}{v_{max}} . \quad (46)$$

with δx_{min} the minimum equivalent diameter of mesh elements, v_{max} the maximum value of the norm of \mathbf{v} .

4.5. Numerical reference velocity for nonlinear simulations

In the nonlinear regime above onset, the order of magnitude of the velocity induced by the buoyancy can be obtained by balancing the inertial and buoyancy terms in Eq. (18):

$$(\mathbf{v} \cdot \nabla)\mathbf{v} \sim RP\theta . \quad (47)$$

As $(\mathbf{v} \cdot \nabla)\mathbf{v} \sim v^2$ and $\theta \sim 1$, one finds a characteristic velocity

$$V_r = \sqrt{RP} . \quad (48)$$

As this velocity V_r may be quite high (~ 100), the components of the vector X (38) may be unbalanced between the temperature and velocity components. Then, the numerical inversion of the linear relation (39) may become unaccurate. To avoid numerical problems in nonlinear simulations, the numerical code calculates the velocity $\tilde{\mathbf{v}} = \mathbf{v}/V_r$. A new inertial unit of time is also chosen, which is the turnover time based on the dimensional velocity corresponding to V_r , and on the length d . Thus, with these new scales, $\tilde{t} = (RP)^{1/2}t$ with the scales of section 2. With these new units, the Eqs. (13) and (18) become

$$\frac{\partial \theta}{\partial \tilde{t}} + \tilde{\mathbf{v}} \cdot \nabla \theta = (RP)^{-1/2} \operatorname{div}(\nabla \theta) + \tilde{\mathbf{v}} \cdot \mathbf{e}_y, \quad (49)$$

$$\frac{\partial \tilde{\mathbf{v}}}{\partial \tilde{t}} + (\tilde{\mathbf{v}} \cdot \nabla)\tilde{\mathbf{v}} = (R/P)^{-1/2} \operatorname{div} \left(-\tilde{\Pi} \bar{\bar{\mathbf{I}}} + \tilde{\bar{\bar{\boldsymbol{\tau}}}} \right) + \theta \mathbf{e}_y, \quad (50)$$

with $\bar{\tau} = \eta \bar{\gamma}$, $\eta = (1 + \tilde{\lambda}^2 \tilde{\gamma}^2)^{(n_i-1)/2}$ and $\tilde{\lambda} = \lambda V_r$. In the code, the weak formulation of (49) and (50), together with the incompressibility condition, is solved internally in the nonlinear runs, but the results are always presented with the dimensionless units defined in section 2. On the contrary, for 'linear' runs near onset, the equations with the dimensionless units of section 2 are used. Indeed, near onset, the velocity estimated using the thermal diffusion time (12) is relevant.

4.6. Initial condition

The first simulations of the code are started with a vanishing temperature field, $\theta_0 = 0$, and a velocity field which corresponds to a divergence-free roll:

$$\mathbf{v}_0 = 16A_0 \left(-\frac{2y}{k}(y-1)(2y-1) \sin(kx) \mathbf{e}_x + y^2(y-1)^2 \cos(kx) \mathbf{e}_y \right), \quad (51)$$

with $k = 3.116$ the dimensionless wavenumber of the critical rolls and A_0 the amplitude of the initial perturbation of the velocity. For parametric studies, to reduce the duration of the transients, a continuation method is used: each new simulation is started with the permanent regime solution corresponding to the closest set of parameters, as an initial condition.

5. Validation of the numerical method

5.1. Mesh and time step

Computations at $R = 1800$ and $P = 7$ for a Newtonian fluid show that the values of the velocity at the middle of the cell height do not vary by more than 0.25% using meshes with 20×20 to 50×50 rectangles. In the following, we will use a mesh of 40×40 rectangles to preserve the accuracy for non-Newtonian calculations and high Rayleigh numbers. The results for strongly shear-thinning fluids have been verified with a mesh of 60×60 rectangles and they differ by less than 0.1%. In the following, we provide the coefficients obtained by fitting our results with an accuracy of four digits to allow accurate comparisons, even if the last digit is one order of magnitude below the error level.

To set the time step $\delta\tilde{t}$, the CFL condition (46) is checked at every time step and $\delta\tilde{t}$ is automatically adjusted to $\delta\tilde{t} = 0.5 \min(\delta x/\tilde{v})$ if $\delta\tilde{t} < 0.1 \min(\delta x/\tilde{v})$ or $\delta\tilde{t} > \min(\delta x/\tilde{v})$. This tolerance range is defined such that one does not have to modify $\delta\tilde{t}$ at every time step. The CFL condition (46) leads to $\delta\tilde{t} \leq 0.025/\tilde{v}_{max}$ with the 40×40 rectangles mesh. As the velocity \tilde{v} has been defined such as $\tilde{v} \sim 1$, $\delta\tilde{t} = 0.01$ is a good initial guess value. To avoid too large $\delta\tilde{t}$ values when the flow velocity collapses to zero, we set $\delta\tilde{t}_{max} = 0.1$ as the maximum allowed value. This insures numerical stability and an acceptable accuracy during the transient from the initial condition to the final static state. In the following, the validation of the numerical code using the well known Newtonian case provides an additional evidence that the time step chosen insures accuracy in the transient stage of the flow. Note also that the final static solution does not depend on the time-step value.

5.2. Comparisons with linear and weakly nonlinear theories

To determine the linear threshold of the primary instability in the Newtonian case, we compute the transient evolution of the velocity and temperature, starting with the initial condition (51) with a very small amplitude $A_0 = 10^{-6}$. We compute the time evolution of the flow at $R = 1700$ and $R = 1715$, *i.e.* around the value of the critical Rayleigh number $R_c = 1707.76$ found by Schlüter *et al.* [3]. From exponential fits of the time series, we extract the linear growth rates $\sigma(R = 1700) = -0.0585245$ and $\sigma(R = 1715) = 0.054549$ at $P = 1$. A linear fit between these values provides a critical value $R_c = 1707.76$ undistinguishable from the Schlüter *et al.* [3] value. Moreover, the linear stability theory provides the characteristic time τ_0 for the instability:

$$\tau_0 = 0.05084 + 0.02601/P = 0.07685 \text{ if } P = 1, \quad (52)$$

such that near onset the growth rate

$$\sigma = \epsilon/\tau_0 . \quad (53)$$

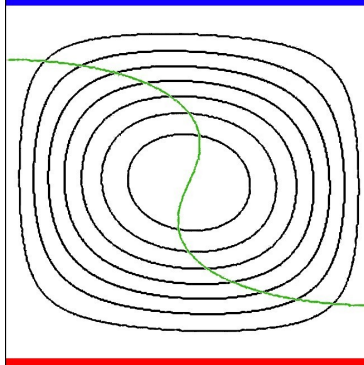


Figure 2: Roll solution in a Newtonian fluid with $P = 1$, $R = 5123$: regularly spaced streamlines (black curves) and isotherm corresponding to the mean temperature T_0 (gray curve - green curve on the web).

The Eqs. (52) and (53) leads to the following values of the growth rate:

$$\sigma(R = 1700) = -0.05913 \text{ and } \sigma(R = 1715) = 0.05517 . \quad (54)$$

These values and those obtained with our code agree within 1.1%.

In a strongly nonlinear regime, at $R = 5123$ and $P = 1$, we find a Nusselt $Nu = 2.12674$ in perfect agreement with the calculation of Plows [4] which gives $Nu = 2.13$. The fields corresponding to this case are shown on Fig. 2. They have been compared with the fields computed with the spectral code of [20], and a perfect agreement has been found.

As already mentioned in the introduction, in principle, in a Carreau fluid the linear instability occurs at the same value of R as in a Newtonian fluid. This has been checked with the Freefem code, using the parameters $n_i = 0.5$ and $\lambda = 0.02$, which correspond to $\alpha = 10^{-4}$. With growth rate computations, we also find $R_c = R_c^{\text{Newt}} = 1707.76$.

Nonlinear results for a Newtonian fluid and this Carreau fluid with $\alpha = 10^{-4}$ are displayed on the Fig. 3. The full curves are tangent to the weakly nonlinear lines given by (28) and (30), which have been obtained independently. The slope of these lines are 1.431 (resp. 2.676) according to Eq. (28) (resp. 30). The coefficients of the linear terms of polynomial fits of degree 11 to the Freefem

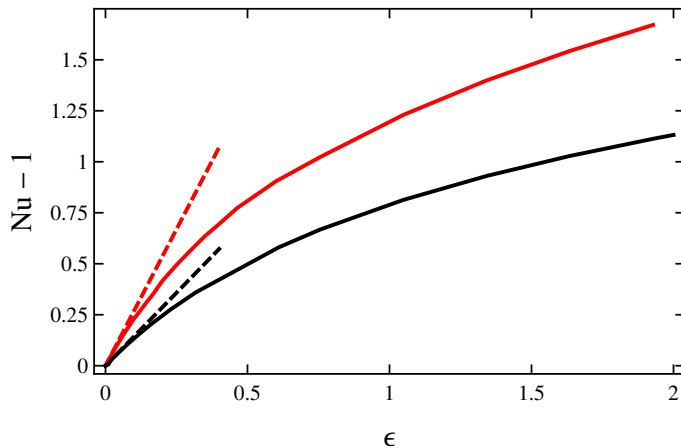


Figure 3: For a Newtonian fluid with $P = 7$ (black) and a Carreau fluid with $P = 7$, $n_i = 0.5$, $\lambda = 0.02$ (gray - red on the web), reduced Nusselt vs distance to onset data. The full curves show the numerical results of the Freefem code, the dashed lines show the weakly nonlinear approximations (28) and (30).

data are 1.444 (resp. 2.727). The relative differences between the slopes given by (28) and (30) and the ones measured by fits of the nonlinear data are 0.9% and 1.9%. This constitutes a validation of our code in the nonlinear, non-Newtonian regime.

6. Subcritical rolls in shear-thinning fluids

6.1. Subcritical rolls

Hereafter we will always use

$$P = 7. \quad (55)$$

According to the weakly nonlinear criterion (27), for $n_i \leq 0.9$ and $\lambda \geq 1$, $\alpha \geq 0.05 > \alpha_c$, hence the bifurcation to rolls is subcritical. Classically, the roll solution branch can then be continued down to a subcritical value R_{sc} where the low Nu , unstable part of this branch merges with the high Nu , presumably stable part of this branch in a saddle-node bifurcation. Below R_{sc} , all roll flows

decay. By following the upper branch numerically, we can estimate R_{sc} . We first compute a solution using a Rayleigh number above R_c , with the initial condition (51), to capture nonlinear rolls. Once a steady solution is obtained, we use it as the initial condition of another computation at a lower Rayleigh number. This process is repeated: we follow the upper branch of roll solution, which appears to be 'stable' at least from a numerical point of view, step-by-step in the Rayleigh number R . When the flow velocity vanishes, *i.e.*, when the Nusselt number tends to 1, it means that $R < R_{sc}$. The step between two successive values of the Rayleigh number is reduced to 5 close to R_{sc} . Therefore, we can estimate in this manner R_{sc} within an error of the order of $\pm 1\%$. Solution branches obtained with this method are displayed on the Figs. 4 and 5. As expected, the subcritical behaviour is stronger when α increases, *i.e.* when n_i decreases or λ increases. In Fig. 9, we observe that the minimal value of R_{sc} is 115.6 for the strongest shear thinning parameters used in our study ($n_i = 0.5$ and $\lambda = 10$), to compare to $R_c = 1707.76$. Indeed, for strongly shear thinning fluids, the viscosity decreases abruptly when the rate of strain increases, *i.e.* subcritical convection is strongly favoured.

6.2. Correlation law for the Nusselt number

According to the weakly nonlinear theory, in the vicinity of the saddle-node bifurcation, the Nusselt number should grow proportionally to $\sqrt{\epsilon_s}$, with

$$\epsilon_s = R/R_{sc} - 1 \tag{56}$$

the relative distance to the subcritical onset. Therefore, in order to propose a correlation law for the Nusselt number of subcritical rolls, we assume a relation of the form:

$$Nu(R, n_i, \lambda) = K(n_i, \lambda)\sqrt{\epsilon_s} + Nu_{sc}(n_i, \lambda). \tag{57}$$

Here, K is a coefficient and $Nu_{sc} > 1$ the Nusselt number at the subcritical Rayleigh number R_{sc} . Fig. 6 confirms, for $n_i = 0.8$, the relevance of the ansatz

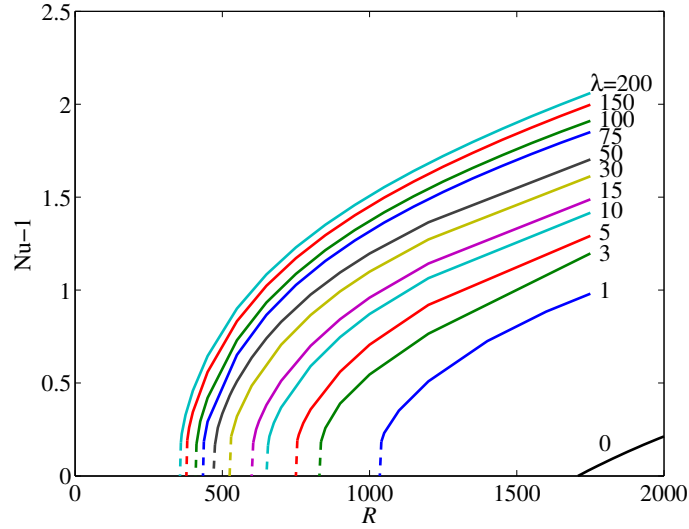


Figure 4: In a Carreau fluid with $P = 7$, $n_i = 0.8$, reduced Nusselt *vs* Rayleigh number for different values of λ as indicated. The full curves connect nonlinear roll solutions. For each λ , the dashed line connects the last non-vanishing solution, in terms of θ , \mathbf{v} or $Nu - 1$, to the conduction solution which is found at the next smaller value of R studied.

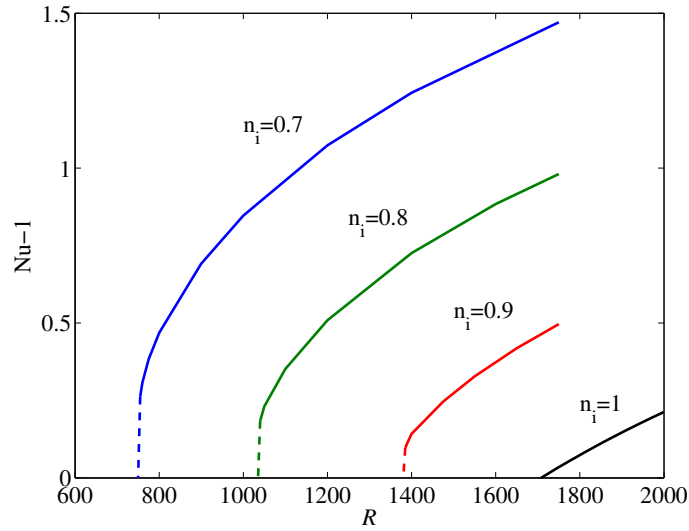


Figure 5: Same as Fig. 4, but for different values of n_i and a fixed value of λ , $\lambda = 1$.

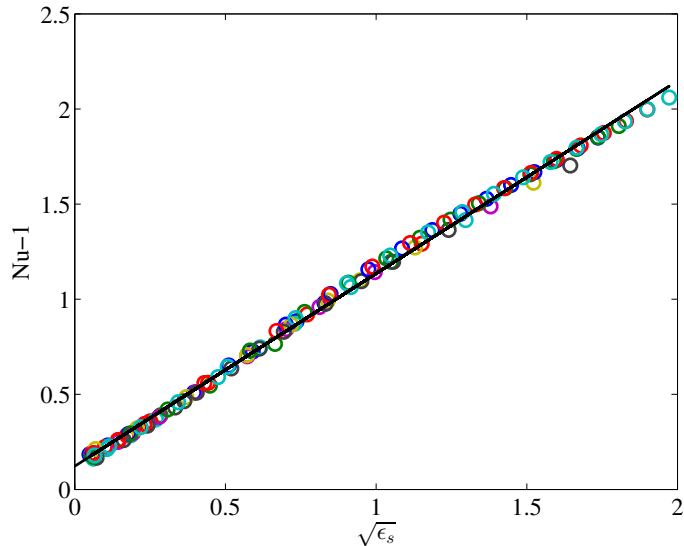


Figure 6: For $n_i = 0.8$, reduced Nusselt numbers of the data of Fig. 4, for $1 \leq \lambda \leq 200$, vs the square root of the relative distance to the subcritical Rayleigh number ϵ_s (Eq. 56). The full line is the linear fit $Nu = 1.0126\sqrt{\epsilon_s} + 1.1222$ (least square residual $r^2 = 0.9980$).

(57). Moreover, it suggests that the coefficients are independent of λ , *i.e.*

$$K(n_i, \lambda) = K(n_i) \quad \text{and} \quad Nu_{sc}(n_i, \lambda) = Nu_{sc}(n_i). \quad (58)$$

In order to determine $K(n_i)$ and $Nu_{sc}(n_i)$, linear regressions are performed, for $\lambda = 1$, with several values of n_i in Fig. 7. The high values of the least square residuals suggest that the law (57) is relevant in the range of rheological parameters used. The values of K and Nu_{sc} are displayed in Figs. 8-a and 8-b. A good agreement is found between the numerical data and the linear fits

$$K(n_i) = -1.2958n_i + 2.0217, \quad Nu_{sc}(n_i) - 1 = -0.9725n_i + 0.9060. \quad (59)$$

The λ -dependence of the Nusselt number in the final form of the correlation

$$Nu(R, n_i, \lambda) = K(n_i)\sqrt{\epsilon_s} + Nu_{sc}(n_i) \quad (60)$$

is contained in $\epsilon_s = R/R_{sc} - 1$. We will now study the subcritical Rayleigh number $R_{sc} = R_{sc}(n_i, \lambda)$.

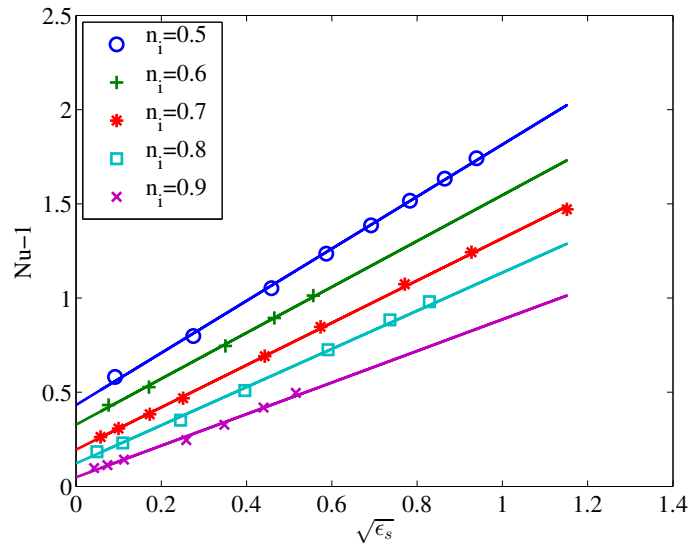


Figure 7: Reduced Nusselt number *vs* the square root of the relative distance to the subcritical Rayleigh number ϵ_s , for $\lambda = 1$ and different values of n_i . The full lines are linear fits using all data points (the least square residuals $0.9935 \leq r^2 \leq 0.9996$).

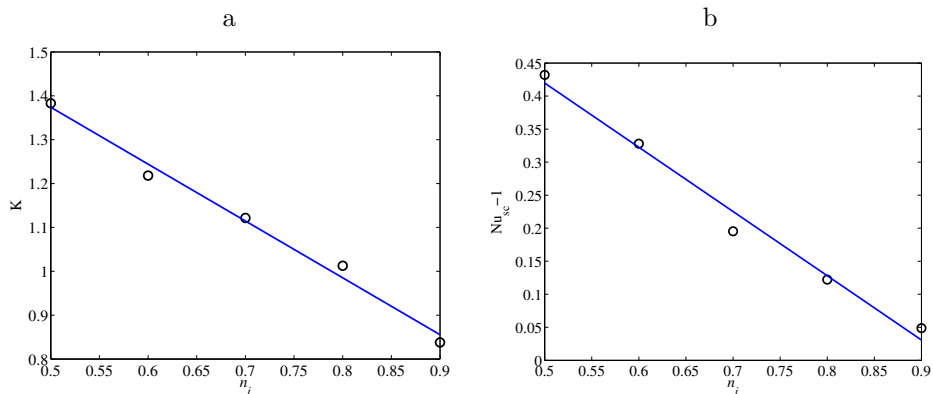


Figure 8: Coefficient K (a) and reduced subcritical Nusselt number (b) *vs* n_i . The full lines show the linear fits (59), the least square residuals $r^2 = 0.9889$ (a) and $r^2 = 0.9851$ (b).

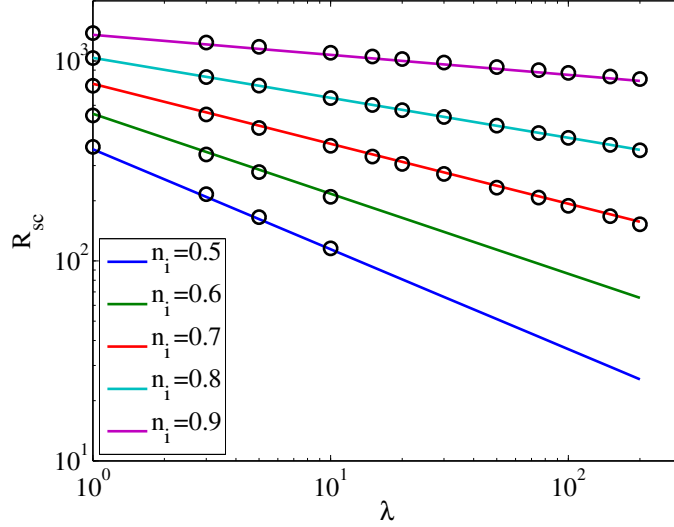


Figure 9: Subcritical Rayleigh number R_{sc} for different values of the shear-thinning index n_i . \circ : numerical data. Full lines use the Eq. (63) and the power law (64) for fitting data.

6.3. Asymptotic power-law regime

The results of Fig. 9 suggest that the subcritical Rayleigh number R_{sc} follows a power law of the form

$$R_{sc}(n_i, \lambda) = R_1(n_i) \lambda^{\gamma(n_i)} \quad (61)$$

for $\lambda \geq 1$. Fits of the data of Fig. 9 to such a power law yield the results of Fig. 10, *i.e.*,

$$\gamma(n_i) = 1.0208n_i - 1.0172. \quad (62)$$

This is quite close to $\gamma(n_i) = n_i - 1$, which would indicate that the Rayleigh number for the corresponding power-law fluid, $Ra_{sc} = \lambda^{1-n_i} R_{sc}$, according to Eq. (11), is constant. Therefore, hereafter we write, instead of (61),

$$R_{sc}(n_i, \lambda) = Ra_{sc}(n_i) \lambda^{n_i-1}, \quad (63)$$

and, by fitting $Ra_{sc}(n_i)$, we extract the data of Fig. 11. Fitting the values of $Ra_{sc}(n_i)$ to a power law of n_i , we obtain, as shown in Fig. 11, a very good interpolation of our numerical data :

$$Ra_{sc}(n_i) = 1710.49 n_i^{2.2411} . \quad (64)$$

This law has been obtained with data in the range $n_i \in [0.5, 0.9]$. It is interesting to note that for, $n_i = 1$, it gives $Ra_{sc}(1) = 1710.49$, which is, naturally, R_c^{Newt} within 0.16%. One can consider our Fig. 11 as a new, more accurate version of the Fig. 20 of [9] (for the 'dragless vertical boundaries' case). The combination of the formulae (63) and (64) yields a rather precise prediction of $R_{sc}(n_i, \lambda)$,

$$R_{sc}(n_i, \lambda) = 1710.49 n_i^{2.2411} \lambda^{n_i-1}, \quad (65)$$

as demonstrated by the Fig. 12.

In fact, the temperature and the velocity fields in the subcritical solutions at $R \simeq R_{sc}$ seem to converge to a given structure, as shows the Fig. 13. This structure should be seen as the one in the power-law fluid case. This convergence happens despite increasing variations of the viscosity, as λ increases. Of course, one can question the relevance of using the zero-rate-of-strain viscosity η_0 in the definition of the Rayleigh number (1), or an approximation of the viscosity at $\dot{\gamma} = \tau_{th}^{-1}$ in the Rayleigh number (11). In the next subsections, we will explore alternate definitions of the viscosities, to define alternate Rayleigh numbers.

6.4. Analysis with the Parmentier's viscosity

Parmentier [11] suggested, on the basis of an analysis of the kinetic energy equation, to define what we call the Parmentier's viscosity,

$$\eta_P = \frac{\int_D \eta \dot{\gamma}^2 d^2x}{\int_D \dot{\gamma}^2 d^2x}, \quad (66)$$

with the notations already defined at the level of Eqs. (31-33). Using the Parmentier-Rayleigh number Ra_P (7) constructed on this viscosity, and all the subcritical solutions at $R \simeq R_{sc}$ that we have computed, we obtain the Fig. 14.

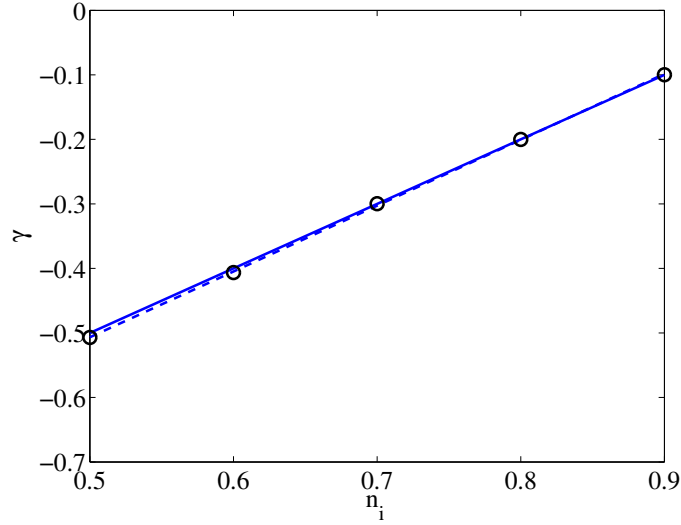


Figure 10: The values of γ plotted by \circ are obtained by fitting the numerical values of the subcritical Rayleigh number R_{sc} using Eq. (61) at each shear-thinning index n_i . The dashed line is the fitted curve $\gamma(n_i) = 1.0208n_i - 1.0172$, least square residual $r^2 = 0.99986$. The full line shows $\gamma(n_i) = n_i - 1$, least square residual $r^2 = 0.99911$.

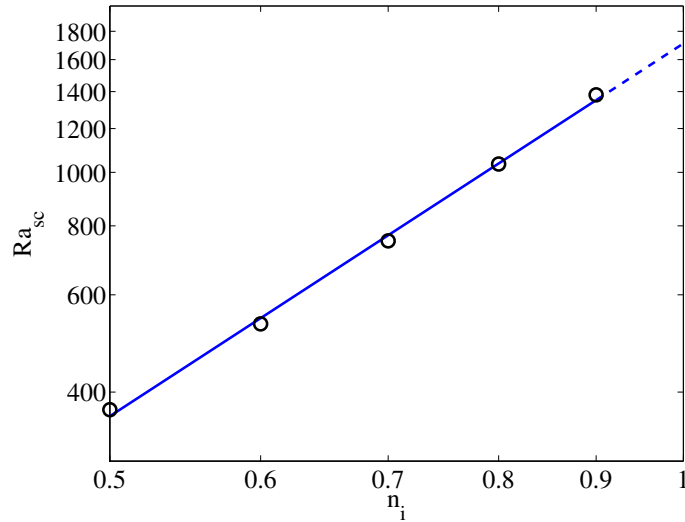


Figure 11: Fit of the power-law Rayleigh number Ra_{sc} with the power law (64); least-square residual $r^2 = 0.99786$.

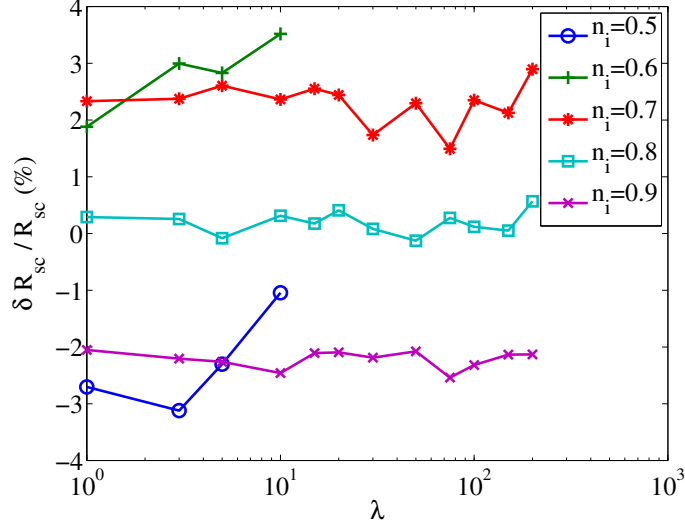


Figure 12: Relative difference between the analytic formula (65) and the numerical subcritical Rayleigh number.

All data collapse on the $Nu(Ra)$ curve for a Newtonian fluid. This confirms the results of Parmentier [11], which were obtained for higher values of Ra_P (denoted \bar{Ra} in his article), $Ra_P \geq 10^4$.

The Fig. 14 shows also that, the smaller the shear-thinning index n_i , the more vigorous is the convection around the saddle-node bifurcation at $R \simeq R_{sc}$: the Nusselt number corresponding to these solutions increases as n_i decreases. This is reasonable, since small n_i correspond to strongly shear-thinning fluids. Clearly, as $n_i \rightarrow 1$, $R_{sc} \rightarrow R_c^{\text{Newt}}$ and the saddle-node solution converges to the bifurcation solution in the Newtonian, supercritical case, *i.e.*, to the static solution, which is characterized by $Nu - 1 = 0$. This is also visible on the Fig. 15. The dispersion of the data points of the Fig. 15 suggests that the Parmentier viscosity, the values of which are plotted on the Fig. 16, is not the one that can collapse the saddle node or subcritical R_{sc} values.

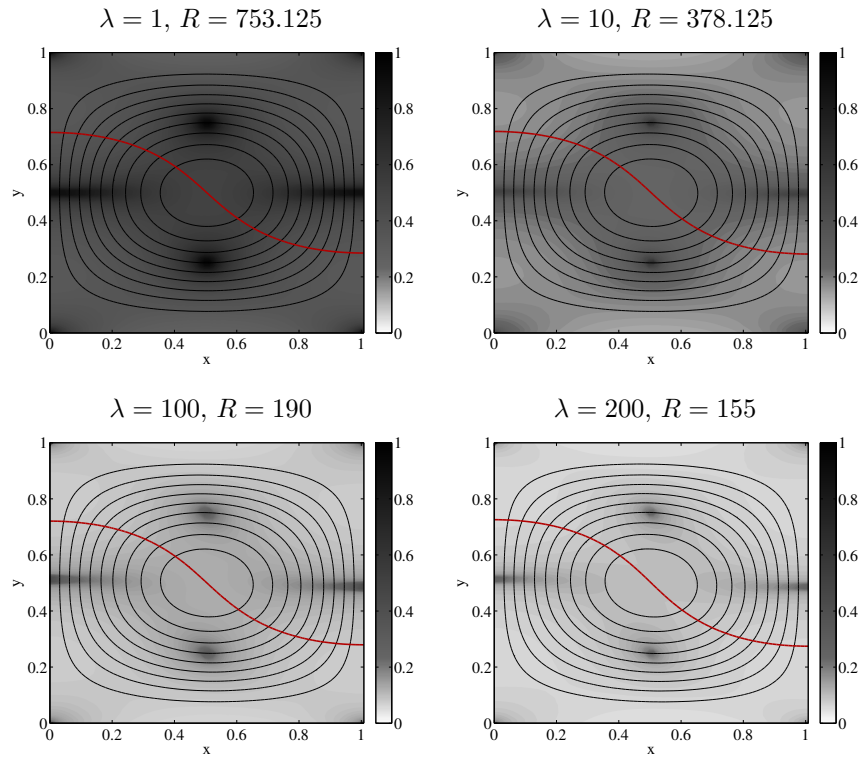


Figure 13: Subcritical roll solutions at $R \simeq R_{sc}$, for $n_i = 0.7$ at different values of λ . The thin black lines are regularly spaced streamlines. The thick line (in gray, red on the web) is the isotherm $T = T_0$. The gray scales show the viscosity field.

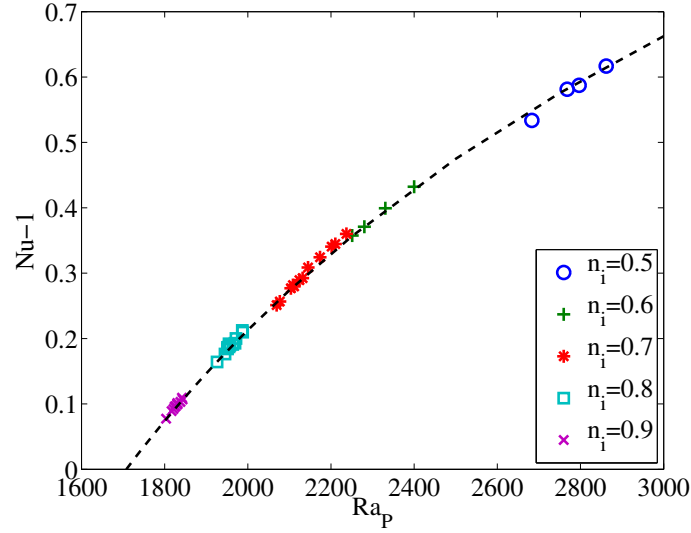


Figure 14: Reduced Nusselt number *vs* the Parmentier-Rayleigh number for the subcritical solutions at $R \simeq R_{sc}$, for all the values of n_i and λ studied. The dashed line shows the reduced Nusselt number *vs* Rayleigh number curve for a Newtonian fluid.

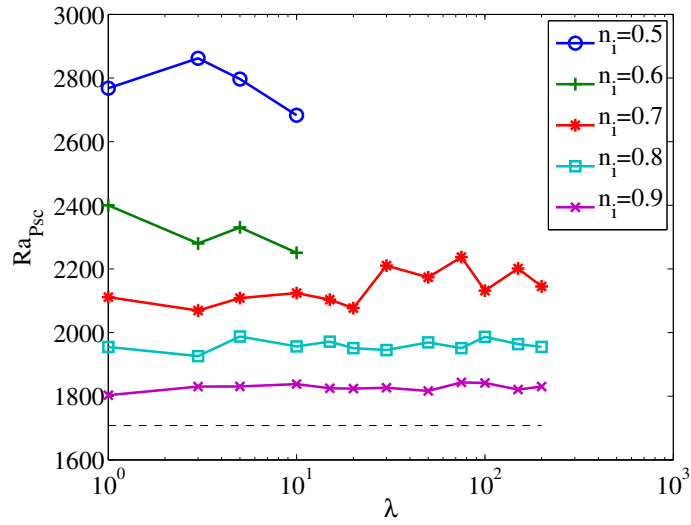


Figure 15: Subcritical Parmentier-Rayleigh number Ra_{Psc} . The dashed line shows $Ra_P = R_c^{Newt}$.

6.5. Analysis with an effective viscosity - Relevance of the average viscosity

We define a dimensionless ‘neutral’ or ‘effective’ viscosity such that the subcritical Rayleigh number constructed on it is constant, equal to the Newtonian critical value:

$$R_c^{\text{Newt}} = \frac{R_{sc}}{\eta_e} \quad i.e. \quad \eta_e = \frac{R_{sc}}{R_c^{\text{Newt}}} . \quad (67)$$

The corresponding dimensional viscosity $\eta_0\eta_e$ can be seen as the viscosity of the equivalent Newtonian fluid that leads to a critical temperature difference $(\delta T)_c$ equal to the subcritical temperature difference $(\delta T)_{sc}$, all the other parameters being the same, *i.e.*, that leads to the ‘same onset’. Using (67) to calculate the effective viscosity in each case, we obtain the results of the Fig. 16, which also display the Parmentier’s viscosity and the bulk-average viscosity

$$\eta_m = \frac{\int_D \eta \, d^2x}{\int_D d^2x} . \quad (68)$$

It is observed that the Parmentier’s viscosity is below the effective viscosity. On the contrary, the values of η_m are found to be close to the effective viscosity η_e . The fact that $\eta_e \simeq \eta_m \ll 1$ at large λ suggests that the reference viscosity (1 in dimensionless units, η_0 in dimensional units) is not the relevant one to characterize the onset of rolls in Rayleigh-Bénard convection of a shear-thinning fluid. Note also that Eqs. (65) and (67) yield an analytic approximation of η_e and η_m , the characteristic viscosity at the onset of subcritical convection,

$$\eta_e \simeq \eta_m \simeq n_i^{2.2411} \lambda^{n_i-1} . \quad (69)$$

7. Influence of a finite viscosity at infinite rate of strain

As shows the Eq. (8), the previous study concerns fluids with a vanishing viscosity, $\eta_\infty = 0$, at infinite rate of strain, $\dot{\gamma} \rightarrow +\infty$. In this section, we

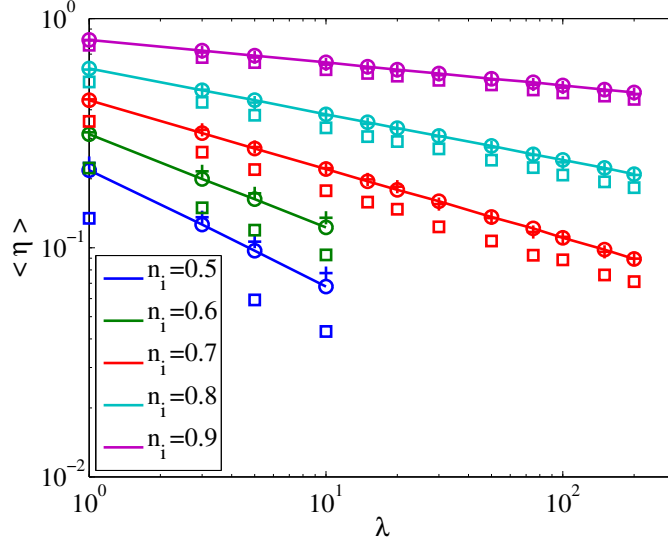


Figure 16: Average and equivalent viscosities for different shear-thinning index n_i . \circ : equivalent viscosity η_e ; \square : Parmentier's viscosity η_P ; $+$: average viscosity η_m .

examine the effect of a finite viscosity $\eta_\infty \neq 0$ at infinite rate of strain, *i.e.*, in dimensionless units, the rheological model (16) is modified as follows:

$$\eta = \eta_\infty + (1 - \eta_\infty) (1 + \lambda^2 \dot{\gamma}^2)^{(n_i - 1)/2} . \quad (70)$$

To validate our numerical method when $\eta_\infty \neq 0$, we compare with [12] for $P = 10$, $n_i = 0.6$, $\lambda = 0.4$, $\eta_\infty = 0.01$, and for an aspect ratio of the cell $L_x/d = 1$, which would not bring significantly different results than with our value $L_x/d = 1.008$. Benouared *et al.* [12] found a subcritical Rayleigh number $R_{sc} = 800$, whereas our computations show that $780 < R_{sc} < 782.5$, which is only 2% smaller. Moreover, the value of Nusselt number at $R = 800$ found by [12] is $Nu = 1.4798$ to compare to our value, $Nu = 1.4751$: the relative difference is smaller than 0.32%. A second point was compared at $R = 2000$, and the relative difference of the Nusselt numbers is 0.38% ($Nu = 2.7759$ for [12] and $Nu = 2.7655$ for us).

The Fig. 17-a shows that increasing the value of η_∞ stabilizes the system,

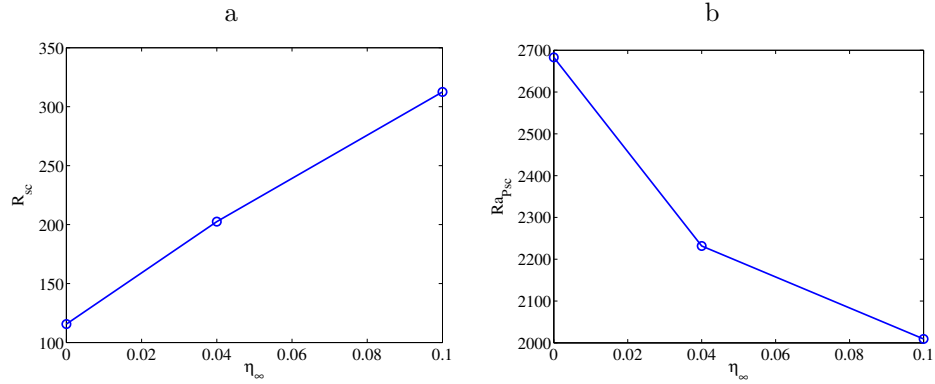


Figure 17: Subcritical Rayleigh number R_{sc} (a) and Parmentier-Rayleigh number Ra_{Psc} (b) for different values of the viscosity η_∞ at $n_i = 0.5$ and $\lambda = 10$.

which is reasonable since this increases the minimum value of the viscosity. However, using the Parmentier’s viscosity as reference viscosity leads to the opposite effect, as shows the Fig. 17-b. Note that, when $\eta_\infty \rightarrow 1$, the fluid becomes Newtonian and $R_{sc} \rightarrow R_c^{\text{Newt}}$, $Ra_{Psc} \rightarrow R_c^{\text{Newt}}$.

By introducing the effective and average viscosities as already defined in Eqs. (67,68), we obtain the Fig. 18. It shows the same tendencies as in the case $\eta_\infty = 0$, *i.e.*, the effective and average viscosities are close, and quite relevant, whereas the Parmentier’s viscosity is smaller.

8. Conclusion

We have confirmed with bidimensionnal, fully nonlinear computations of roll solutions in Carreau fluids that the transition to thermoconvection flows in strongly shear-thinning fluids is subcritical. The subcritical onset of convection and the corresponding subcritical solutions have been characterized for $P \gtrsim 1$. The threshold value of the Rayleigh number R_{sc} , based on the viscosity η_0 of the fluid in the static state, decreases when the shear-thinning increases, which suggests that somehow the shear-thinning ‘destabilizes’ the system. However, further analysis using the Parmentier’s viscosity η_P [11] to define the Rayleigh number shows that when the shear-thinning index n_i decreases (Fig. 14), the

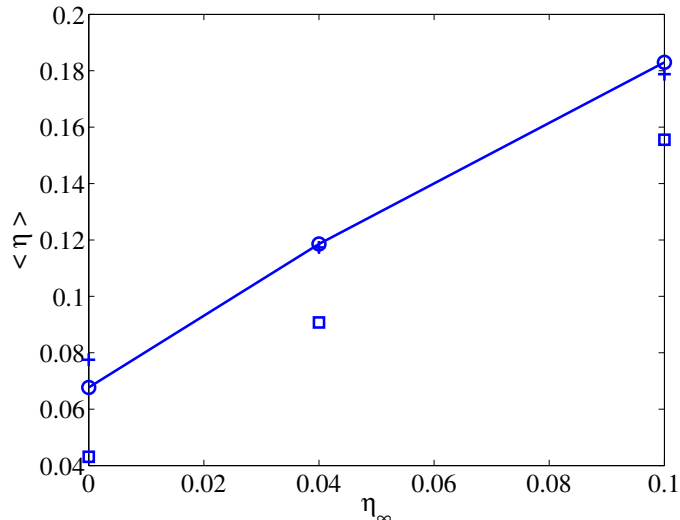


Figure 18: Average and equivalent viscosities for different viscosities η_∞ at $n_i = 0.5$ and $\lambda = 10$. ○ : equivalent viscosity η_e ; □ : Parmentier's viscosity η_P ; + : average viscosity η_m .

shear-thinning ‘stabilizes’ the conductive state, *i.e.*, it increases the critical value of the Parmentier-Rayleigh number Ra_{Psc} . Finally, we have defined a neutral or effective viscosity η_e , such that the subcritical Rayleigh number based on it is always equal to R_c^{Newt} . This effective viscosity, which corresponds to the one of an equivalent Newtonian fluid at onset (see after Eq. 67), is close to the bulk-average viscosity η_m , even if the viscosity at infinite rate of strain $\eta_\infty \neq 0$. This rather simple result, and the fact that the temperature and velocity fields at onset of subcritical convection are close to the ones in Newtonian rolls (see the Fig. 13), shows that somehow the rheology of the viscous fluids considered here does not influence strongly the structure of thermoconvection rolls.

In the case $\eta_\infty = 0$, where the fluid behaves, as soon as it is sufficiently shear-thinning, like a power-law fluid, a correlation for the Nusselt number Nu vs R , up to $R \sim 2000$ at least, is proposed in Eqs. (59) and (60) for the subcritical cases $0.5 \leq n_i \leq 0.9$ and $1 \leq \lambda < +\infty$. In the limit $\lambda \rightarrow +\infty$, because $R = Ra \lambda^{n_i-1}$ and $R_{sc} = Ra_{sc}(n_i)\lambda^{n_i-1}$, the Eq. (60) gives a correlation for

the Nusselt number of a power-law fluid, $Nu = Nu(Ra, n_i)$, with ϵ_s calculated as $Ra/Ra_{sc}(n_i) - 1$. To calculate the subcritical Rayleigh numbers, power laws have been derived for both R_{sc} and Ra_{sc} (Eqs. 64 and 65) and also for the characteristic viscosity (Eq. 69). The correlation (60) and the power-law (64) for the onset of convection might be useful for some Engineering problems with power-law fluids.

It should be pointed out that in the present study we considered a periodic geometry and two spatial dimensions only. It would be interesting to develop two-dimensional computations in a less constrained geometry, and, also, three-dimensional computations. This would allow a systematic study of the stability of subcritical rolls *vs* general perturbations. Another extension of this work could consider more complex rheological models. One might want to take into account temperature effects on the viscous parameters for instance. Finally, it would be interesting to study a thixotropic model that extends naturally the Carreau model, like the one of [21].

Acknowledgements

We thank François Sirvente & Rémi Chemin, students of Mines Nancy, Department Energy: Production, Transformation, for their contributions. It is within this Department that A. Briard started this work. We thank Chérif Nouar for useful input; Dr. Mahmoud Mamou for drawing our attention on the work [12], and for communicating some of his results.

This work has been supported by the French National Agency (ANR) in the frame of the research project *Thermoconvective instabilities for microstructured fluids* (ThIM), ANR-10-BLAN-0925-01.

References

- [1] E. Bodenschatz, W. Pesch, G. Ahlers, Recent developments in Rayleigh-Bénard convection, *Annu. Rev. Fluid Mech.* 32 (2000) 709–778.

- [2] G. Ahlers, S. Grossmann, D. Lohse, Heat transfer and large scale dynamics in turbulent Rayleigh-Bénard convection, *Rev. Mod. Phys.* 81 (2009) 503–537. doi:10.1103/RevModPhys.81.503.
- [3] A. Schlüter, D. Lortz, F. Busse, On the stability of steady finite amplitude convection, *J. Fluid Mech.* 23 (1965) 129–144.
- [4] W. Plows, Some numerical results for two-dimensional steady laminar Bénard convection, *Phys. Fluids* 11 (1968) 1593–1599.
- [5] R. Larson, Instabilities in viscoelastic flows, *Rheologica Acta* 31 (1992) 213–263. doi:10.1007/BF00366504.
- [6] P. Kolodner, Oscillatory convection in viscoelastic DNA suspensions, *J. Non-Newt. Fluid Mech.* 75 (1998) 167 – 192. doi:10.1016/S0377-0257(97)00095-5.
- [7] M. Darbouli, C. Métivier, J.-M. Piau, A. Magnin, A. Abdelali, Rayleigh-Bénard convection for viscoplastic fluids, *Phys. Fluids* 25 (2013) 023101. doi:10.1063/1.4790521.
- [8] Z. Kebiche, C. Castelain, T. Burghelca, Experimental investigation of the Rayleigh-Bénard convection in a yield stress fluid, *J. Non-Newt. Fluid Mech.* 203 (2014) 9 – 23. doi:10.1016/j.jnnfm.2013.10.005.
- [9] H. Ozoe, S. W. Churchill, Hydrodynamic stability and natural convection in Ostwald-de Waele and Ellis fluids: The development of a numerical solution, *AIChE Journal* 18 (1972) 1196–1207.
- [10] H. Ozoe, S. W. Churchill, Hydrodynamic stability and natural convection in Newtonian and non-Newtonian fluids heated from below, *AIChE Symposium Ser.* 69 (1973) 126–133.
- [11] E. Parmentier, Study of thermal convection in non-Newtonian fluids, *J. Fluid Mech.* 84 (1) (1978) 1–11.

- [12] O. Benouared, M. Mamou, N. A. Messaoudene, Numerical nonlinear analysis of subcritical Rayleigh-Bénard convection in a horizontal confined enclosure filled with non-Newtonian fluids, *Phys. Fluids* 26 (2014) 073101. doi:10.1063/1.4890829.
- [13] J. P. Carreau, Rheological equations from molecular network theories, *J. Rheol.* 16 (1972) 99–127.
- [14] R. Bird, R. Armstrong, O. Hassager, Dynamics of polymeric liquids, Wiley - Interscience, New York, 1987.
- [15] N. J. Balmforth, A. C. Rust, Weakly nonlinear viscoplastic convection, *J. Non-Newt. Fluid Mech.* 158 (2009) 36 – 45. doi:10.1016/j.jnnfm.2008.07.012.
- [16] B. Albaalbaki, R. E. Khayat, Pattern selection in the thermal convection of non-Newtonian fluids, *J. Fluid Mech.* 668 (2011) 500–550.
- [17] M. Bouteraa, C. Nouar, E. Plaut, C. Métivier, A. Kalck, Weakly nonlinear analysis of Rayleigh-Bénard convection in shear-thinning fluids: nature of the bifurcation and pattern selection, submitted (revised version) to the *J. Fluid Mech.*
- [18] F. Hecht, New development in freefem++, *J. Numer. Math.* 20 (3-4) (2012) 251–265.
- [19] J. Cahouet, J. Chabard, Some fast 3-D solvers for the generalized Stokes problem, *Int. J. Numer. Methods Fluids* 8 (1988) 869–895.
- [20] E. Plaut, F. H. Busse, Low-Prandtl-number convection in a rotating cylindrical annulus, *J. Fluid Mech.* 464 (2002) 345–363.
- [21] S. Boi, A. Mazzino, J. O. Pralits, Minimal model for zero-inertia instabilities in shear-dominated non-Newtonian flows, *Phys. Rev. E* 88 (2013) 033007. doi:10.1103/PhysRevE.88.033007.

Appendix A. Freefem++ source code

The algorithm to compute the subcritical Rayleigh number has been withdrawn from the code, to make it easier to be read and used.

```
// Begin of the program

real ttgv=1e30; // very large value
real ttpv=1e-6; // very small value

// Mesh and time parameters

real dt=0.01; // Time step
int np=40; // Number of points along x
int mp=40; // Number of points along y
int N=100000; // Number of time steps
int frequenceSauvegarde=50; // Skip step for saving

// Physical parameters

real kx=3.116; // No slip wave number
real x0 = 0;
real x1 = 0.5*2*pi/kx;
real y0=0;
real y1=1;

real Pr=7; // Prandtl number

// Internal reference velocity
real Vref;
real tref;

// Viscosity parameters
real eta0=1.0;
```

```

real etainf=0.0;
real etamoy, gmoy, mumoy;

real nc=0.8;
real lambda=1.0;
real a=2;

real alpha=1./dt;
real nn=1./mp;

real Nu=1; // Nusselt number
real Nuo=20;
real dNu;
real temps; // Time

real adh=0; // No slip velocity
real imp=0; // Normal velocity

mesh Th;

fespace VVh(Th, [P2,P2,P2]);
VVh [v1,v2,t], [f1,f2,f3];
// [v1,v2,t] velocity and temperature
// [f1,f2,f3] test function

fespace Vh(Th,P2);
Vh v1o,v2o,to,nu,g2;
// [v1o,v2o,to] old velocity and temperature
// nu viscosity
// g2 second invariant of the strain rate tensor

fespace VMh(Th, [P1]);

```

```

fespace Mh(Th,P1);
Mh p,pw;
// p pressure
// pw working pressure

// Name of reading and writting files
string inputf;
string outputf;

real Rainputf=1750; // Reading file Rayleigh number
real Ra=1750; // Rayleigh number

real ifrst=0; // Boolean for reading files
real nLoad=nc; // Shearthinning index for reading file
real lLoad=lambda; // lambda for reading file

if(ifrst) inputf="N"+nLoad+"L"+lLoad+"/Ra"+Rainputf;

Vref=sqrt(Ra*Pr);
tref=1./Vref;

// Warning : Saving folder must be created BEFORE running the script
// Example :
// Create a folder named such as N0.8L1 in the working directory
outputf="N"+nc+"L"+lambda+"/Ra"+Ra;

// Core of the program

// Mesh generation or reading
if (ifrst)
{
    Th=readmesh(inputf+"ThRef.msh");
}

```

```

}
else
{
    Th = square(np,mp,[x0+(x1-x0)*x,y0+(y1-y0)*y]);
}

// Reading of starting files
if (ifrst)
{
    {
        ifstream file(inputf+"vt.txt"); // Velocity and temperature
        file>>v1[];
    }
    {
        ifstream file(inputf+"p.txt"); // Pressure
        file>>p[];
    }
    {
        ifstream file(inputf+"temps.txt"); // Time
        file>>temps;
    }
    {
        ifstream file(inputf+"dt.txt"); // Time step
        file>>dt;
    }
    ttpv=-abs(ttpv);
    alpha=1./dt;
}
else
{ // Start from scratch
    temps=0;
    p=0;
    [v1,v2,t]=[-0.1*32*y/kx*(y-y1)*(2*y-y1)*sin(kx*x),0.1*16*y^2*(y-y1)^2*cos(kx*x),0];
}

```

```

}

savemesh(Th,outputf+"ThRef.msh"); // Save mesh

macro gamma(v1,v2) (2*dx(v1)^2+2*dy(v2)^2+(dx(v2)+dy(v1))^2) // 2th invariant

// Viscosity law (Carreau)
macro eta(v1,v2)
((etainf+(eta0-etainf)*(1+(Vref*lambda)^a*(gamma(v1,v2))^(a/2))^(nc-1)/a)/eta0) //

plot(Th,wait=1,cmm="Maillage");
if(ifrst)
{
    plot(t,wait=1,cmm="Temperature. Time="+temps);
}
nu=eta(v1,v2);
plot(nu,fill=1,wait=1,cmm="Viscosity. Time="+temps);

macro div(v1,v2) (dx(v1)+dy(v2)) // divergence

varf vDiv([v1,v2,t],[q],qforder=4)=int2d(Th)(div(v1,v2)*q);
matrix MDiv=vDiv(VVh,VMh);

macro grad(u) [dx(u),dy(u)] // gradient

// Problem definition

problem vRBnn([v1,v2,t],[f1,f2,f3],solver=CG,eps=ttpv)=
    int2d(Th)(alpha*(v1*f1 + v2*f2 + t*f3)
+ (Pr*tref)*nu*(2*dx(v1)*dx(f1)+2*dy(v2)*dy(f2)
+ (dy(v1)+dx(v2))*(dy(f1)+dx(f2)))
+ tref*(dx(t)*dx(f3)+dy(t)*dy(f3)))
- int2d(Th)(f1*(alpha*v1o-[v1o,v2o] '*grad(v1o))

```

```

        +f2*(alpha*v2o-[v1o,v2o]’*grad(v2o))
        +f3*(alpha*to-[v1o,v2o]’*grad(to))
+ div(f1,f2)*pw
+ (Ra*Pr*tref^2)*to*f2
+ v2o*f3)
+ on(1,3,v1=adh,v2=adh,t=0) + on(2,4,v1=imp);

// Function divup
func real[int] divup(real[int] & pp)
{ pw[]=pp;
  vREnn;
  real[int] divu=MDiv*v1[];
  return divu;
};

//Preconditionner
varf vA(p,q) = int2d(Th)((grad(p)’*grad(q)));
varf vM(p,q) = int2d(Th,qft=qf2pT)(p*q);
matrix pAM=vM(Mh,Mh,solver=UMFPACK);
matrix pAA=vA(Mh,Mh,solver=UMFPACK);

real vism=0.5*(1.5*nu[] .min+0.5)*tref*Pr;

func real[int] Precon(real[int] & p)
{
  real[int] pa= pAA^-1*p;
  real[int] pm= pAM^-1*p;
  real[int] pp= alpha*pa+vism*pm;

  return pp;
}

int res;

```

```

real dtc;
nu=eta(v1,v2);
v1o=v1;
v2o=v2;
to=t;

int i=1;
dNu=1;

while (dNu>1e-5 && i<=N)
{
    i++;
    temps+=dt;
    cout << "temps=" << temps << " dt=" << dt << endl;
    vism=0.5*(1.5*nu[].min+0.5)*tref*Pr;
    res=LinearCG(divup,p[],precon=Precon,veps=ttpv,nbiter=50,verbosity=10);
    assert(res==1);
    ttpv=-abs(ttpv);
    divup(p[]);
    v1o=v1;
    v2o=v2;
    to=t;
    nu=eta(v1,v2);

    cout << " v1 max " << v1[].linfty
        << " v2 max " << v2[].linfty
        << " t max " << t[].linfty
        << " visc min " << nu[].min << endl;

    // CFL Condition for dt
    pw=hTriangle/sqrt(v1^2+v2^2);
    dtc=pw[].min;
    if(dt>dtc)

```

```

        {dt=0.5*dtc;
        alpha=1./dt;
        cout << "dt change to " << dt << " CFL limit " << dtc << endl;}
if(dt<0.1*dtc)
    {dt=min(0.5*dtc,0.05);
    alpha=1./dt;
    cout << "dt change to " << dt << " CFL limit " << dtc << endl;}

// Nusselt number
Nu=int1d(Th,3,qfe=qf2pE)(-dy(t));

// Saving temporal data
{ofstream ff(outputf+"Nu_t.txt",append); ff << temps << " " << Nu << endl;};
plot([v1,v2],value=true,wait=0,cmm="[v1,v2] au temps = "+temps);

// Saving full fields
if(i%frequenceSauvegarde==0)
{
    dNu=abs(Nu-Nuo)/dt;
    Nuo=Nu;
    {ofstream f(outputf+"vt.txt");
    ofstream g(outputf+"p.txt");
    ofstream h(outputf+"temps.txt");
    ofstream l(outputf+"dt.txt");
    f << v1[]; // [v1,v2,t]
    g << p[]; // pressure
    h << temps;
    l << dt;
    };
}
};// End of the time loop

// Average viscosities

```

```

etamoy=int2d(Th)(nu);
etamoy*=1./((x1-x0)*(y1-y0));
{ofstream ff(outputf+"visco.txt",append); ff << " mean visc. = " << etamoy << endl;};
g2=gamma(v1,v2);
etamoy=int2d(Th)(nu*g2);
gmoy=int2d(Th)(g2);
mumoy=etamoy/gmoy;
{ofstream ff(outputf+"mup.txt",append);
ff << etamoy << " " << gmoy << " " << mumoy << endl;};

// Final saving
{
ofstream f(outputf+"vt.txt");
ofstream g(outputf+"p.txt");
ofstream h(outputf+"temps.txt");
ofstream l(outputf+"dt.txt");
f<< v1[]; // [v1,v2,v3,t]
g<<p[]; // pressure
h<<temps;
l<<dt;
}

{ofstream ff("N"+nc+"L"+lambda+"/NuN"+nc+"L"+lambda+".txt",append);
ff << Ra << " " << Nu << " " << i << " " << dNu << endl;};

// End of the program

```